

Si x emission lines in spectra obtained with the *Solar EUV Rocket Telescope and Spectrograph (SERTS)*

F. P. Keenan,¹★ E. O'Shea,¹ R. J. Thomas,² J. W. Brosius,³ A. Katsiyannis,¹
R. S. I. Ryans,¹ R. H. G. Reid,⁴ A. K. Pradhan⁵ and H. L. Zhang⁶

¹Department of Pure and Applied Physics, Queen's University, Belfast BT7 1NN

²Laboratory for Astronomy and Solar Physics, Code 682, NASA/Goddard Space Flight Center, Greenbelt, MD 20771, USA

³Raytheon ITSS, Code 682, NASA/Goddard Space Flight Center, Greenbelt, MD 20771, USA

⁴Department of Applied Mathematics and Theoretical Physics, Queen's University, Belfast BT7 1NN

⁵Department of Astronomy, Ohio State University, 174 West 18th Avenue, Columbus, OH 43210-1106, USA

⁶Applied Theoretical and Computational Physics Division, Los Alamos National Laboratory, Los Alamos, NM 87545, USA

Accepted 1999 October 4. Received 1999 August 12

ABSTRACT

New **R**-matrix calculations of electron impact excitation rates for transitions among the $2s^22p$, $2s2p^2$ and $2p^3$ levels of Si x are presented. These data are subsequently used, in conjunction with recent estimates for proton excitation rates, to derive theoretical electron density sensitive emission-line ratios involving transitions in the ~ 253 – 356 Å wavelength range. A comparison of these with observations of a solar active region and subflare, obtained during the 1989 flight of the *Solar EUV Rocket Telescope and Spectrograph (SERTS)*, reveals that the electron densities determined from most of the Si x line ratios are consistent with one another for both solar features. In addition, the derived densities are also in good agreement with the values of N_e estimated from diagnostic lines in other species formed at similar electron temperatures to Si x, such as Fe xii and Fe xiii. These results provide observational support for the general accuracy of the adopted atomic data, and hence line ratio calculations, employed in the present analysis. However, we find that the Si x 256.32-Å line is blended with the He ii transition at the same wavelength, while the feature at 292.25 Å is not due to Si x, but currently remains unidentified. The intensity of the 253.81-Å line in the *SERTS* active region spectrum is about a factor of 3 larger than expected from theory, but the reason for this is unclear, and requires additional observations to explain the discrepancy.

Key words: atomic data – Sun: activity – Sun: flares – ultraviolet: general.

1 INTRODUCTION

Emission lines arising from $2s^22p$ – $2s2p^2$ transitions in boron-like Si x have been frequently observed in solar extreme-ultraviolet spectra (see, for example, Vernazza & Reeves 1978; Dere 1982). Recently, Si x transitions have also been detected in the *Extreme-Ultraviolet Explorer* satellite spectra of the star ξ Bootis A (Laming & Drake 1999). The diagnostic potential of these lines was first noted by Flower & Nussbaumer (1975a), who presented electron density and temperature sensitive emission-line ratios for Si x, calculated using electron impact excitation rates derived in the ‘distorted wave’ approximation (Eissner & Seaton 1972). Since then, several authors have produced theoretical line ratios for Si x applicable to solar spectra, mostly calculated using distorted wave atomic data (see Keenan 1996 and references therein).

In this paper we present electron excitation rates for Si x, calculated using the **R**-matrix method of Burke & Robb (1975), which are subsequently employed to derive electron density sensitive line ratios for this ion. We investigate the usefulness and accuracy of these diagnostics through a comparison with solar observational data from the *Solar EUV Rocket Telescope and Spectrograph (SERTS)*.

2 ELECTRON IMPACT EXCITATION RATES

Electron impact excitation rates for transitions in Si x have been calculated by Zhang, Graziani & Pradhan (1994) and Zhang & Pradhan (1994), using the **R**-matrix code as adapted for the Opacity Project (Berrington et al. 1987; Seaton 1987), and extended for the Iron Project (Hummer et al. 1993). Relativistic effects were incorporated into the **R**-matrix results through the term-coupling method (Eissner, Jones & Nussbaumer 1974).

★ E-mail: f.keenan@qub.ac.uk

Table 1. Index of Si x levels.

Index	Level	Energy (Ryd) ^a
1	2s ² 2p ² P _{1/2}	0.000 000
2	2s ² 2p ² P _{3/2}	0.063 703
3	2s2p ² ⁴ P _{1/2}	1.467 231
4	2s2p ² ⁴ P _{3/2}	1.489 831
5	2s2p ² ⁴ P _{5/2}	1.522 363
6	2s2p ² ² D _{3/2}	2.623 082
7	2s2p ² ² D _{5/2}	2.623 356
8	2s2p ² ² S _{1/2}	3.350 456
9	2s2p ² ² P _{1/2}	3.554 306
10	2s2p ² ² P _{3/2}	3.590 666
11	2p ³ ⁴ S _{3/2}	4.641 357
12	2p ³ ² D _{3/2}	5.243 704
13	2p ³ ² D _{5/2}	5.243 887
14	2p ³ ² P _{1/2}	5.893 711
15	2p ³ ² P _{3/2}	5.899 452

^aFrom Martin & Zalubas (1983).

However, Zhang et al. only listed Si x excitation rates for a small number of transitions, while Zhang & Pradhan provided results at only a single temperature for three transitions, and even these are slightly incorrect due to an error when including the term-coupling coefficients. The index to the transitions is given in Table 1, and in Table 2 we therefore list the (corrected) atomic data for all 105 fine-structure transitions among the 2s²2p, 2s2p² and 2p³ levels, for a range of electron temperatures over which Si x has a fractional abundance in ionization equilibrium of $N(\text{Si x})/N(\text{Si}) > 10^{-3}$ (Mazzotta et al. 1998). These data are given in the form of effective collision strengths Y , which are related to the excitation rate coefficients C (in units of $\text{cm}^3 \text{s}^{-1}$) by the expression

$$C_{ij} = \frac{8.63 \times 10^{-6}}{g_i \sqrt{T_e}} Y_{ij} \exp(-E_{ij}/kT_e),$$

Table 2. Effective collision strengths for transitions in Si x.

T_e (K)	Transition key ^a							
	1 2	1 3	1 4	1 5	1 6	1 7	1 8	1 9
	1 10	1 11	1 12	1 13	1 14	1 15	2 3	2 4
	2 5	2 6	2 7	2 8	2 9	2 10	2 11	2 12
	2 13	2 14	2 15	3 4	3 5	3 6	3 7	3 8
	3 9	3 10	3 11	3 12	3 13	3 14	3 15	4 5
	4 6	4 7	4 8	4 9	4 10	4 11	4 12	4 13
	4 14	4 15	5 6	5 7	5 8	5 9	5 10	5 11
	5 12	5 13	5 14	5 15	6 7	6 8	6 9	6 10
	6 11	6 12	6 13	6 14	6 15	7 8	7 9	7 10
	7 11	7 12	7 13	7 14	7 15	8 9	8 10	8 11
	8 12	8 13	8 14	8 15	9 10	9 11	9 12	9 13
	9 14	9 15	10 11	10 12	10 13	10 14	10 15	11 12
	11 13	11 14	11 15	12 13	12 14	12 15	13 14	13 15
	14 15							
8.100+5 ^b	5.62–1 ^b	1.99–2	3.01–2	2.23–2	5.61–1	3.99–2	3.39–1	5.13–1
	3.04–1	7.18–4	6.73–3	4.56–3	4.40–3	3.81–3	1.58–2	4.14–2
	8.50–2	1.43–1	9.72–1	3.03–1	4.66–1	1.65–0	1.38–3	6.23–3
	1.47–2	4.52–3	1.39–2	1.78–1	1.26–1	4.77–2	2.91–2	1.02–2
	5.84–3	9.93–3	4.41–1	1.54–2	1.96–3	3.81–3	2.09–3	3.55–1
	7.43–2	8.01–2	1.92–2	1.17–2	2.19–2	9.02–1	2.09–2	1.38–2
	6.00–3	6.94–3	6.36–2	1.71–1	2.66–2	1.84–2	3.68–2	1.39–0
	4.10–3	4.72–2	3.69–3	1.80–2	3.47–1	8.88–2	1.63–1	1.70–1
	2.82–3	1.16–0	1.98–1	5.69–1	1.42–1	1.43–1	1.07–1	3.78–1
	4.33–3	2.29–1	1.91–0	8.52–3	9.42–1	5.68–2	1.38–1	9.12–4
	5.19–2	3.56–3	1.26–1	5.89–1	2.47–1	2.28–2	1.11–0	1.05–2
	8.01–1	1.46–1	4.72–2	1.97–1	1.83–0	3.26–1	1.79–0	9.51–2
	1.42–1	2.62–2	5.21–2	1.91–1	8.18–2	1.08–1	7.72–2	2.10–1
	7.36–2							
1.134+6	4.57–1	1.79–2	2.67–2	1.92–2	5.52–1	3.43–2	3.41–1	5.14–1
	3.02–1	6.68–4	6.68–3	4.48–3	4.37–3	3.71–3	1.37–2	3.62–2
	7.53–2	1.34–1	9.47–1	3.02–1	4.68–1	1.65–0	1.29–3	6.11–3
	1.45–2	4.41–3	1.37–2	1.56–1	1.11–1	4.36–2	2.64–2	9.38–3
	4.89–3	8.62–3	4.37–1	1.48–2	1.85–3	3.66–3	2.00–3	3.12–1
	6.78–2	7.30–2	1.77–2	1.00–2	1.90–2	8.97–1	2.00–2	1.31–2
	5.75–3	6.66–3	5.77–2	1.56–1	2.45–2	1.63–2	3.17–2	1.40–0
	3.83–3	4.51–2	3.53–3	1.73–2	2.83–1	8.32–2	1.27–1	1.39–1
	2.18–3	1.14–0	1.92–1	5.68–1	1.41–1	1.32–1	8.92–2	2.97–1
	3.32–3	2.27–1	1.88–0	8.23–3	9.41–1	4.49–2	1.07–1	8.09–4
	5.08–2	2.78–3	1.24–1	5.76–1	2.07–1	1.99–2	1.08–0	9.03–3
	7.85–1	1.43–1	4.12–2	1.89–1	1.78–0	3.20–1	1.75–0	8.87–2
	1.33–1	2.43–2	4.83–2	1.77–1	8.20–2	1.07–1	7.58–2	2.09–1
	6.88–2							
1.620+6	3.64–1	1.60–2	2.36–2	1.65–2	5.39–1	2.94–2	3.38–1	5.10–1
	2.98–1	6.18–4	6.59–3	4.37–3	4.31–3	3.58–3	1.17–2	3.15–2
	6.63–2	1.25–1	9.16–1	2.99–1	4.67–1	1.63–0	1.19–3	5.97–3
	1.43–2	4.27–3	1.34–2	1.35–1	9.83–2	3.93–2	2.37–2	8.46–3

Table 2 – *continued*

	4.06–3	7.42–3	4.28–1	1.39–2	1.71–3	3.46–3	1.89–3	2.72–1
	6.10–2	6.55–2	1.59–2	8.47–3	1.63–2	8.83–1	1.89–2	1.23–2
	5.44–3	6.29–3	5.18–2	1.40–1	2.22–2	1.43–2	2.71–2	1.39–0
	3.53–3	4.25–2	3.33–3	1.63–2	2.29–1	7.90–2	9.65–2	1.12–1
	1.65–3	1.12–0	1.84–1	5.62–1	1.39–1	1.24–1	7.37–2	2.30–1
	2.50–3	2.23–1	1.84–0	7.87–3	9.34–1	3.49–2	8.14–2	7.15–4
	4.91–2	2.15–3	1.21–1	5.58–1	1.73–1	1.73–2	1.04–0	7.79–3
	7.61–1	1.38–1	3.58–2	1.79–1	1.71–0	3.12–1	1.69–0	8.16–2
	1.22–1	2.22–2	4.40–2	1.62–1	8.25–2	1.05–1	7.44–2	2.09–1
	6.33–2							
T_e (K)								
2.106+6	3.07–1	1.46–2	2.14–2	1.47–2	5.24–1	2.62–2	3.33–1	5.02–1
	2.93–1	5.79–4	6.50–3	4.28–3	4.25–3	3.47–3	1.05–2	2.84–2
	6.01–2	1.19–1	8.87–1	2.95–1	4.62–1	1.61–0	1.11–3	5.85–3
	1.40–2	4.15–3	1.32–2	1.20–1	9.02–2	3.61–2	2.17–2	7.76–3
	3.54–3	6.62–3	4.18–1	1.32–2	1.60–3	3.28–3	1.79–3	2.47–1
	5.60–2	6.01–2	1.46–2	7.48–3	1.46–2	8.65–1	1.79–2	1.16–2
	5.15–3	5.97–3	4.76–2	1.29–1	2.04–2	1.30–2	2.42–2	1.37–0
	3.30–3	4.02–2	3.15–3	1.54–2	1.96–1	7.71–2	7.92–2	9.57–2
	1.35–3	1.09–0	1.78–1	5.54–1	1.37–1	1.20–1	6.41–2	1.90–1
	2.03–3	2.19–1	1.79–0	7.54–3	9.22–1	2.90–2	6.64–2	6.52–4
	4.75–2	1.80–3	1.18–1	5.40–1	1.53–1	1.56–2	1.00–0	7.00–3
	7.38–1	1.33–1	3.24–2	1.72–1	1.64–0	3.03–1	1.64–0	7.61–2
	1.14–1	2.05–2	4.07–2	1.51–1	8.30–2	1.04–1	7.33–2	2.09–1
	5.91–2							
2.835+6	2.54–1	1.31–2	1.91–2	1.29–2	5.03–1	2.30–2	3.24–1	4.89–1
	2.84–1	5.29–4	6.36–3	4.15–3	4.14–3	3.32–3	9.21–3	2.51–2
	5.35–2	1.12–1	8.47–1	2.87–1	4.51–1	1.56–0	1.01–3	5.68–3
	1.37–2	3.99–3	1.28–2	1.05–1	8.24–2	3.24–2	1.95–2	6.93–3
	3.02–3	5.80–3	4.03–1	1.22–2	1.47–3	3.03–3	1.65–3	2.21–1
	5.02–2	5.39–2	1.30–2	6.46–3	1.28–2	8.37–1	1.65–2	1.07–2
	4.76–3	5.53–3	4.28–2	1.16–1	1.82–2	1.15–2	2.11–2	1.33–0
	3.01–3	3.72–2	2.91–3	1.43–2	1.66–1	7.55–2	6.33–2	8.00–2
	1.07–3	1.05–0	1.69–1	5.39–1	1.32–1	1.17–1	5.46–2	1.54–1
	1.60–3	2.11–1	1.72–0	7.07–3	8.99–1	2.34–2	5.27–2	5.84–4
	4.53–2	1.48–3	1.13–1	5.16–1	1.34–1	1.39–2	9.56–1	6.16–3
	7.05–1	1.27–1	2.87–2	1.62–1	1.56–0	2.91–1	1.57–0	6.93–2
	1.04–1	1.84–2	3.66–2	1.37–1	8.34–2	1.02–1	7.19–2	2.09–1
	5.39–2							
4.050+6	2.03–1	1.13–2	1.64–2	1.09–2	4.70–1	1.94–2	3.07–1	4.63–1
	2.67–1	4.61–4	6.10–3	3.94–3	3.93–3	3.10–3	7.78–3	2.13–2
	4.58–2	1.02–1	7.86–1	2.72–1	4.28–1	1.47–0	8.83–4	5.40–3
	1.31–2	3.74–3	1.21–2	8.90–2	7.41–2	2.79–2	1.68–2	5.90–3
	2.47–3	4.87–3	3.78–1	1.08–2	1.29–3	2.69–3	1.46–3	1.92–1
	4.32–2	4.63–2	1.11–2	5.35–3	1.07–2	7.88–1	1.46–2	9.50–3
	4.22–3	4.90–3	3.70–2	9.95–2	1.56–2	9.81–3	1.76–2	1.26–0
	2.64–3	3.30–2	2.57–3	1.27–2	1.37–1	7.35–2	4.85–2	6.42–2
	8.03–4	9.78–1	1.55–1	5.10–1	1.24–1	1.13–1	4.48–2	1.19–1
	1.19–3	1.97–1	1.60–0	6.35–3	8.52–1	1.81–2	3.99–2	5.03–4
	4.20–2	1.17–3	1.05–1	4.78–1	1.15–1	1.18–2	8.85–1	5.21–3
	6.56–1	1.18–1	2.45–2	1.49–1	1.44–0	2.71–1	1.46–0	6.05–2
	9.05–2	1.58–2	3.13–2	1.19–1	8.27–2	9.89–2	6.91–2	2.05–1
	4.72–2							

^a Index to levels given in Table 1.^b Electron temperatures and effective collision strengths written in the form $A \pm B$, which implies $A \times 10^{\pm B}$.

where T_e is the electron temperature in kelvin, E_{ij} is the energy difference between levels i and j as obtained from Table 1, g_i is the statistical weight of the lower level and k is Boltzmann's constant. We estimate that the results in Table 2 should be accurate to typically ± 10 per cent for transitions among the $2s^2 2p$ levels, and between $2s^2 2p$ and $2s 2p^2$, decreasing to ± 20 – 50 per cent for excitation to the $2p^3$ and among the $2s 2p^2$ and $2p^3$ levels, the degradation in accuracy generally following the excitation energy of the upper level (Zhang et al. 1994).

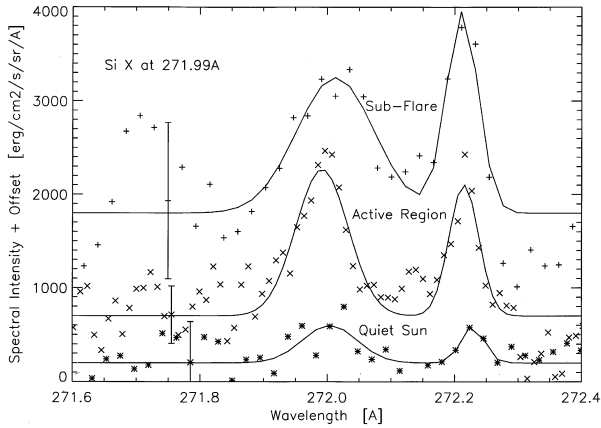
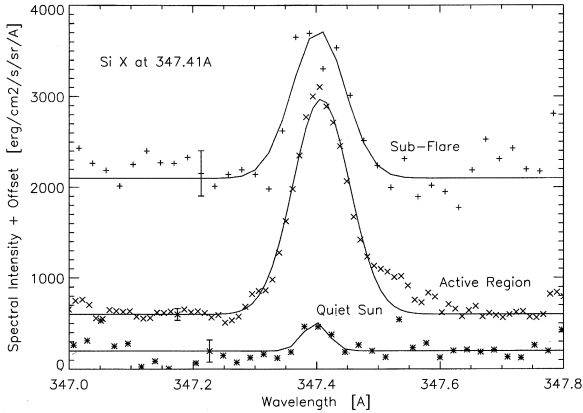
3 OBSERVATIONAL DATA

The solar spectra analysed in the present paper are those of an active region and a small subflare, recorded on Eastman Kodak 101–07 emulsion by *SERTS* during a rocket flight on 1989 May 5 at 17:50 UT (Neupert et al. 1992). The observations cover the wavelength regions 235.46–448.76 Å in first order and 170–224.38 Å in second order (the short-wavelength cut-off in the latter being due to an absorption edge in the thin aluminium filter installed to reduce stray light), with a spatial resolution of about

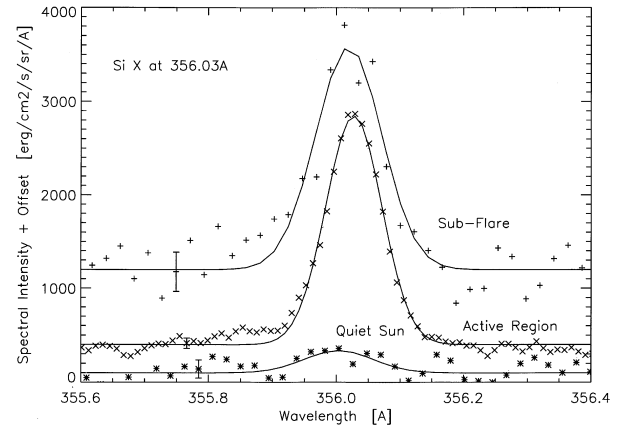
Table 3. Si x transitions in the 1989 May 5 *SERTS* observations (*SERTS*-89).

Transition	$\lambda(\text{\AA})$	$R = I(\lambda)/I(356.03 \text{\AA})$		Ratio
		Active region ^a	Subflare ^b	designation
$2s^2 2p^2 \text{ } ^2\text{P}_{1/2} - 2s 2p^2 \text{ } ^2\text{P}_{3/2}$	253.81	0.950 ± 0.275	—	R_1
$2s^2 2p^2 \text{ } ^2\text{P}_{1/2} - 2s 2p^2 \text{ } ^2\text{P}_{1/2}$	256.32	7.25 ± 1.19	11.51 ± 2.25	R_2
$2s^2 2p^2 \text{ } ^2\text{P}_{3/2} - 2s 2p^2 \text{ } ^2\text{P}_{3/2}$	258.37	1.73 ± 0.33	1.50 ± 0.54	R_6
$2s^2 2p^2 \text{ } ^2\text{P}_{3/2} - 2s 2p^2 \text{ } ^2\text{P}_{1/2}$	261.05	0.642 ± 0.144	—	R_7
$2s^2 2p^2 \text{ } ^2\text{P}_{1/2} - 2s 2p^2 \text{ } ^2\text{S}_{1/2}$	271.99	0.601 ± 0.134	0.704 ± 0.331	R_3
$2s^2 2p^2 \text{ } ^2\text{P}_{3/2} - 2s 2p^2 \text{ } ^2\text{S}_{1/2}$	277.27	0.523 ± 0.129	0.540 ± 0.205	R_8
$2s 2p^2 \text{ } ^4\text{P}_{5/2} - 2p^3 \text{ } ^4\text{S}_{3/2}$	292.25	0.200 ± 0.064	—	R_4
$2s^2 2p^2 \text{ } ^2\text{P}_{1/2} - 2s 2p^2 \text{ } ^2\text{D}_{3/2}$	347.41	0.963 ± 0.246	0.566 ± 0.127	R_5
$2s^2 2p^2 \text{ } ^2\text{P}_{3/2} - 2s 2p^2 \text{ } ^2\text{D}_{3/2,5/2}$	356.03	—	—	—

^a $I(356.03 \text{\AA}) = 270 \pm 31 \text{ erg cm}^{-2} \text{ s}^{-1} \text{ sr}^{-1}$, based on the revised absolute calibration scale.

^b $I(356.03 \text{\AA}) = 311 \pm 45 \text{ erg cm}^{-2} \text{ s}^{-1} \text{ sr}^{-1}$, based on the revised absolute calibration scale.

Figure 1. Plot of the *SERTS*-89 active region and subflare spectra in the wavelength interval 271.6–272.4 Å, containing the Si x 271.99-Å line, as well as an unidentified feature at 272.21 Å. Also shown are the *SERTS*-89 measurements of the quiet Sun in this wavelength range. The best-fitting Gaussian profiles to the emission lines are given, as are typical error bars on an observational data point.

Figure 2. Plot of the *SERTS*-89 active region and subflare spectra in the wavelength interval 347.0–347.8 Å, containing the Si x 347.41-Å line, along with the *SERTS*-89 measurements of the quiet Sun in this wavelength range. The best-fitting Gaussian profiles to the emission lines are also shown, as are typical error bars on an observational data point.

7 arcsec (FWHM) and a spectral resolution of better than 80 mÅ (FWHM) in first order and ≤ 40 mÅ in second. The active region measurements used here were spatially averaged over the central 4.6 arcmin of the spectrograph slit, whereas the subflare results come from a 22-arcsec portion of the same data set.


Figure 3. Plot of the *SERTS*-89 active region and subflare spectra in the wavelength interval 355.6–356.4 Å, containing the Si x 356.03-Å line, along with the *SERTS*-89 measurements of the quiet Sun in this wavelength range. The best-fitting Gaussian profiles to the emission lines are also shown, as are typical error bars on an observational data point.

The Si x transitions identified in the *SERTS*-89 spectra are listed in Table 3. Intensities of these features were determined by fitting Gaussian profiles to microdensitometer scans of the recorded spectra, as discussed by Thomas & Neupert (1994), where details of the wavelength and radiometric calibration of the instrument may also be found. The intensities of the 356.03-Å line in the two solar features are listed in Table 3; the observed intensities of the other Si x transitions may be inferred from these using the line ratios given in the table (see Section 4). Observational uncertainties in the line ratios, which average 24 and 33 per cent for the active region and subflare, respectively, have been determined using methods discussed in detail by Thomas & Neupert. A recent re-evaluation of the absolute calibration scale for *SERTS*-89 increases all active region intensities by a factor of 1.24 over the values reported by Thomas & Neupert, and has been incorporated in the present work.

The quality of the observational data is illustrated in Figs 1–3, where we plot the active region and subflare spectra in the ranges 271.6–272.4, 347.0–347.8 and 355.6–356.4 Å, respectively. Also shown for comparison in the figures are *SERTS*-89 measurements of the quiet Sun in these wavelength ranges, which we note are of too low a quality for reliable Si x line ratios to be derived.

4 THEORETICAL LINE RATIOS

The model ion for Si x consisted of the 15 energetically lowest

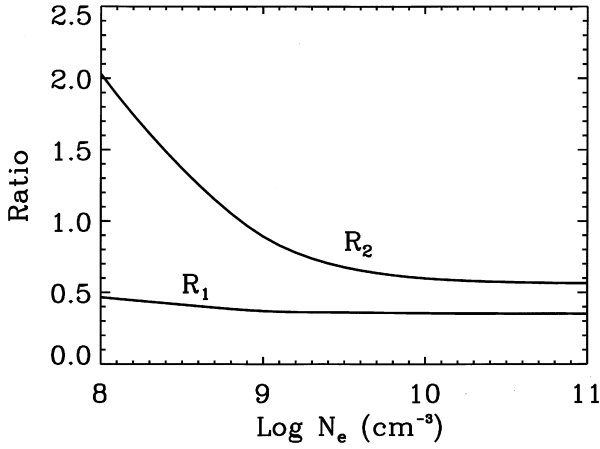


Figure 4. The theoretical Si x emission-line ratios $R_1 = I(253.81 \text{ \AA})/I(356.03 \text{ \AA})$ and $R_2 = I(256.32 \text{ \AA})/I(356.03 \text{ \AA})$, where I is in energy units, plotted as a function of electron density at the temperature of maximum Si x fractional abundance in ionization equilibrium, $\log T_e = \log T_{\max} = 6.1$ (Mazzotta et al. 1998).

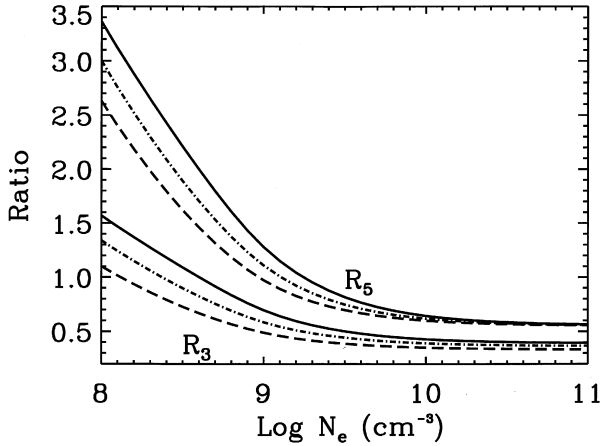


Figure 5. The theoretical Si x emission-line ratios $R_3 = I(271.99 \text{ \AA})/I(356.03 \text{ \AA})$ and $R_5 = I(347.41 \text{ \AA})/I(356.03 \text{ \AA})$, where I is in energy units, plotted as a function of electron density at three electron temperatures, namely $\log T_e = 5.9$ (dashed line), $\log T_e = 6.1$ (dot-dashed line) and $\log T_e = 6.3$ (solid line).

fine-structure levels, which are listed in Table 1. Also given are the energies for these levels, from Martin & Zalubas (1983).

Electron impact excitation rates for transitions in Si x were derived from the effective collision strengths listed in Table 2, while for Einstein A-coefficients the calculations of Galavís, Mendoza & Zeippen (1998) were adopted. The accuracy of the latter should be similar to that for the electron rates, i.e. ± 10 per cent. As noted by, for example, Seaton (1964), excitation by protons will be important for the $2s^2 2p^2 \text{ } ^2P_{1/2} - 2s^2 2p^2 \text{ } ^2P_{3/2}$ transition, and in the present analysis we have used the rates of Foster, Keenan & Reid (1997). However, Flower & Nussbaumer (1975b) have pointed out that proton excitation should additionally be included for the $2s 2p^2 \text{ } ^4P_J - 2s 2p^2 \text{ } ^4P_{J'}$ transitions, and for these rates we have also adopted the calculations of Foster et al. (1997). Both sets of proton rates should be accurate to ± 10 per cent.

Using the atomic data discussed above in conjunction with the statistical equilibrium code of Dufton (1977), relative Si x level populations and hence emission-line intensity ratios were derived

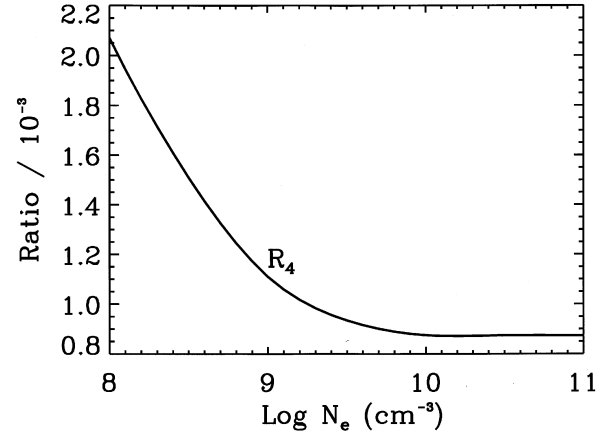


Figure 6. The theoretical Si x emission-line ratio $R_4 = I(292.25 \text{ \AA})/I(356.03 \text{ \AA})$, where I is in energy units, plotted as a function of electron density at the temperature of maximum Si x fractional abundance in ionization equilibrium, $\log T_e = \log T_{\max} = 6.1$ (Mazzotta et al. 1998).

for a range of electron temperatures and densities. Details of the procedures involved and approximations made may be found in Dufton (1977) and Dufton et al. (1978).

In Figs 4–6 we plot the emission-line ratios $R_1 = I(253.81 \text{ \AA})/I(356.03 \text{ \AA})$, $R_2 = I(256.32 \text{ \AA})/I(356.03 \text{ \AA})$, $R_3 = I(271.99 \text{ \AA})/I(356.03 \text{ \AA})$, $R_4 = I(292.25 \text{ \AA})/I(356.03 \text{ \AA})$ and $R_5 = I(347.41 \text{ \AA})/I(356.03 \text{ \AA})$ as a function of electron density at the temperature of maximum Si x fractional abundance in ionization equilibrium, $\log T_e = \log T_{\max} = 6.1$ (Mazzotta et al. 1998). An inspection of the figures reveals that R_2 , R_3 , R_4 and R_5 are sensitive to variations in the electron density, varying by factors of between 2.2 and 5.4 over the density interval $N_e = 10^8 - 10^{11} \text{ cm}^{-3}$. Hence they should provide useful N_e diagnostics. However R_1 is relatively density-insensitive, changing by only 24 per cent between $N_e = 10^8$ and 10^{11} cm^{-3} . We note that the R_1 to R_5 ratios do not vary significantly with temperature. As shown in Fig. 5, reducing the adopted temperature from $\log T_e = 6.1$ to 5.9 leads to changes in R_3 and R_5 of <19 and <14 per cent, respectively. Given the uncertainties in the adopted atomic data (see above and Section 2), we estimate that the results in Figs 4–6 should be accurate to ± 15 per cent.

The ratios $R_6 = I(258.37 \text{ \AA})/I(356.03 \text{ \AA})$, $R_7 = I(261.05 \text{ \AA})/I(356.03 \text{ \AA})$ and $R_8 = I(277.27 \text{ \AA})/I(356.03 \text{ \AA})$ have the same temperature and density dependence as R_1 , R_2 and R_3 , respectively, owing to common upper levels, but with $R_6 = 5.35R_1$, $R_7 = 0.971R_2$ and $R_8 = 0.909R_3$.

5 RESULTS AND DISCUSSION

In Table 4 we summarize the electron densities derived by combining the observed values of R_2 , R_3 , R_4 , R_5 , R_7 and R_8 from Table 3 with the calculations in Figs 4–6 for $\log T_e = \log T_{\max} = 6.1$ (Mazzotta et al. 1998), where the error bars in $\log N_e$ are based on the uncertainties in the line ratio measurements. An inspection of the table reveals that the observed values of R_2 and R_4 in the active region and subflare are greater than the theoretical low-density limit. These discrepancies were previously pointed out by Young, Landi & Thomas (1998), who noted that the 256.32-Å line in the R_2 ratio is blended with the strong He II 256.32-Å transition. Further evidence for this is provided in Table 5, where we see that

Table 4. Si x logarithmic electron densities.

Ratio	$\log N_e(R)$	
	Active region	Subflare
R_2	L^a	L
R_3	$9.0^{+0.3}_{-0.3}$	$8.8^{+1.7}_{-0.4}$
R_4	L	–
R_5	$9.1^{+0.4}_{-0.2}$	≥ 9.7
R_7	$9.5^{+1.9}_{-0.4}$	–
R_8	$9.1^{+0.4}_{-0.3}$	$9.0^{+1.8}_{-0.4}$
Mean density	9.2 ± 0.2	10.3 ± 0.5

^aIndicates that the observed ratio is larger than the theoretical low-density limit.

Table 5. Si x density-insensitive ratios.

Ratio	Observed		Theoretical
	Active region	Subflare	
R_1/R_6	0.549 ± 0.169	–	0.187
R_2/R_7	11.29 ± 2.55	–	1.03
R_3/R_8	1.15 ± 0.33	0.883 ± 0.502	1.10
R_1	0.950 ± 0.275	–	0.361^a
R_6	1.73 ± 0.33	1.54 ± 0.54	1.93^a

^aRatios calculated for $N_e = 10^{9.5} \text{ cm}^{-3}$; $\log T_e = \log T_{\text{max}} = 6.1$ (Mazzotta et al. 1998).

the $I(256.32 \text{ \AA})/I(261.05 \text{ \AA})$ ratio ($= R_2/R_7$) is much larger than the theoretical value, which is both temperature- and density-insensitive. The observed R_4 ratio is more than two orders of magnitude larger than expected from Fig. 6, indicating that the 292.25-Å line is not due to Si x, as also previously noted by Young et al. This feature has also been detected in solar flare spectra from the *Skylab* mission (Dere 1978). An inspection of line lists reveals no obvious candidate for the 292.25-Å line. Observations of this transition in a laboratory spectrum would be of great help in identifying the line (see, for example, Lippmann et al. 1987).

Electron densities deduced from the R_3 , R_5 , R_7 and R_8 ratios in Table 4 are consistent, giving a mean value of $\log N_e = 9.2 \pm 0.2$ for the active region. In the case of the subflare, the derived densities have large error bars, reflecting the fact that the observational uncertainties are greater for the subflare than for the active region (see Section 3). However, the firm lower limit to $\log N_e$ from R_5 means that we can constrain the average density in the subflare to $\log N_e = 10.3 \pm 0.5$. These mean densities are in good agreement with the values determined from diagnostic ratios in species formed at similar temperatures to Si x. For example, Keenan et al. (1996) found $\log N_e = 9.7 \pm 0.4$ and 9.9 ± 0.5 for this same active region and subflare, respectively, from *SERTS*-89 line ratios in Fe xii, which has $\log T_{\text{max}} = 6.1$ (Mazzotta et al. 1998). Similarly, Brickhouse, Raymond & Smith (1995) deduced $\log N_e = 9.5$ for this active region from Fe xiii, with $\log T_{\text{max}} = 6.2$. These results provide experimental support for the accuracy of the atomic data and theoretical diagnostics presented in this paper. They may therefore be applied with confidence to other solar and stellar high-resolution spectra, such as those from the *Solar and Heliospheric Observatory* mission (Harrison et al. 1997).

In Table 5 we summarize both theoretical and experimental values of the ratios R_1 , R_6 , R_1/R_6 , R_2/R_7 and R_3/R_8 . These either are predicted to be insensitive to the adopted plasma parameters (temperature and density), owing to the relevant lines arising from

common upper levels, or (in the case of R_1 and R_6) do not vary significantly with T_e and N_e . Hence they are useful for investigating either blending or the reliability of the instrument calibration (Neupert & Kastner 1983). An inspection of the table reveals excellent agreement between theory and observation for $R_3/R_8 = I(271.99 \text{ \AA})/I(277.27 \text{ \AA})$ and $R_6 = I(258.37 \text{ \AA})/I(356.03 \text{ \AA})$, with discrepancies that are smaller than the experimental uncertainties in the ratios, hence providing support for the theoretical results. However, the disagreements between theory and observation are large for $R_1 = I(253.81 \text{ \AA})/I(356.03 \text{ \AA})$, $R_1/R_6 = I(253.81 \text{ \AA})/I(258.37 \text{ \AA})$ and $R_2/R_7 = I(256.32 \text{ \AA})/I(261.05 \text{ \AA})$. The R_2/R_7 discrepancy has already been discussed by us, and the good agreement found for R_6 implies that the problems with the other ratios must lie with the 253.81-Å line measurement. Errors in the line intensity calculations are unlikely to be responsible, as Young et al. (1998) point out that Malinovsky & Heroux (1973) measure $R_1/R_6 = 0.19$ for the quiet Sun, while Dere (1982) found $R_1/R_6 = 0.22$ for an active region. This suggests that the *SERTS* measurement of the 253.81-Å line is in error. However a re-inspection of the *SERTS* spectrum indicates that the line is well resolved, and should be accurately measured. Clearly, further observations of this transition are required to resolve this puzzle.

ACKNOWLEDGMENTS

EOS and RSIR are grateful to PPARC for financial support. AKP and HLZ acknowledge partial support from the US National Science Foundation (AST 9870089) for the Iron Project. The *SERTS* rocket programme was funded under NASA RTOP 879–11–38. This work was also supported by the Royal Society, the Leverhulme Trust and NATO travel grant CRG.930722.

REFERENCES

- Berrington K. A., Burke P. G., Butler K., Seaton M. J., Storey P. J., Taylor K. T., Yu Y., 1987, *J. Phys. B*, 20, 6379
- Burke P. G., Robb W. D., 1975, *Adv. At. Mol. Phys.*, 11, 143
- Brickhouse N. C., Raymond J. C., Smith B. W., 1995, *ApJS*, 97, 551
- Dere K. P., 1978, *ApJ*, 221, 1062
- Dere K. P., 1982, *Sol. Phys.*, 77, 77
- Dufton P. L., 1977, *Comput. Phys. Commun.*, 13, 25
- Dufton P. L., Berrington K. A., Burke P. G., Kingston A. E., 1978, *A&A*, 62, 111
- Eissner W., Jones M., Nussbaumer H., 1974, *Comput. Phys. Commun.*, 8, 270
- Eissner W., Seaton M. J., 1972, *J. Phys. B*, 5, 2187
- Flower D. R., Nussbaumer H., 1975a, *A&A*, 45, 349
- Flower D. R., Nussbaumer H., 1975b, *A&A*, 45, 145
- Foster V. J., Keenan F. P., Reid R. H. G., 1997, *At. Data Nucl. Data Tables*, 67, 99
- Galavís M. E., Mendoza C., Zeippen C. J., 1998, *A&AS*, 131, 499
- Harrison R. A. et al., 1997, *Sol. Phys.*, 170, 123
- Hummer D. G., Berrington K. A., Eissner W., Pradhan A. K., Saraph H. E., Tully J. A., 1993, *A&A*, 279, 298
- Keenan F. P., 1996, *Space Sci. Rev.*, 75, 537
- Keenan F. P., Thomas R. J., Neupert W. M., Foster V. J., Brown P. J. F., Tayal S. S., 1996, *MNRAS*, 278, 773
- Laming J. M., Drake J. J., 1999, *ApJ*, 516, 324
- Lippmann S., Finkenthal M., Huang L. K., Moos H. W., Stratton B. C., Yu T. L., Bhatia A. K., Hodge W. L., 1987, *ApJ*, 316, 819
- Malinovsky M., Heroux L., 1973, *ApJ*, 181, 1009
- Martin W. C., Zalubas R., 1983, *J. Phys. Chem. Ref. Data*, 12, 323

Mazzotta P., Mazzitelli G., Colafrancesco S., Vittorio N., 1998, A&AS, 133, 403
 Neupert W. M., Epstein G. L., Thomas R. J., Thompson W. T., 1992, Sol. Phys., 137, 87
 Neupert W. M., Kastner S. O., 1983, A&A, 128, 181
 Seaton M. J., 1964, MNRAS, 127, 191
 Seaton M. J., 1987, J. Phys. B, 20, 6563

Thomas R. J., Neupert W. M., 1994, ApJS, 91, 461
 Vernazza J. E., Reeves E. M., 1978, ApJS, 37, 485
 Young P. R., Landi E., Thomas R. J., 1998, A&A, 329, 291
 Zhang H. L., Graziani M., Pradhan A. K., 1994, A&A, 283, 319
 Zhang H. L., Pradhan A. K., 1994, Phys. Rev. A, 50, 3105

This paper has been typeset from a \LaTeX file prepared by the author.